Time-spliced X-ray diffraction imaging of magnetism dynamics in a NdNiO₃ thin film

Kenneth R. Beyerlein[a,b,1]

[a]Condensed Matter Dynamics Department, Max Plank Institute for the Structure and Dynamics of Matter, 22761 Hamburg, Germany; and [b]Center for Free-Electron Laser Science, 22761 Hamburg, Germany

Diffraction imaging of nonequilibrium dynamics at atomic resolution is becoming possible with X-ray free-electron lasers. However, there are unresolved problems with applying this method to objects that are confined in only one dimension. Here I show that reliable one-dimensional coherent diffraction imaging is possible by splicing together images recovered from different time delays in an optical pump X-ray probe experiment. The time and space evolution of antiferromagnetic order in a vibrationally excited complex oxide heterostructure is recovered from time-resolved measurements of a resonant soft X-ray diffraction peak. Midinfrared excitation of the substrate is shown to lead to a demagnetization front that propagates at a velocity exceeding the speed of sound, a critical observation for the understanding of driven phase transitions in complex condensed matter.

coherent X-ray diffraction imaging | resonant X-ray diffraction | midinfrared laser | oxide heterostructure | antiferromagnetism

A growing trend in science and technology involves the use of advanced imaging techniques to study the nonequilibrium evolution of matter (1–3). X-ray free-electron lasers promise a full mapping of ultrafast dynamics, which can be achieved by time-resolved coherent X-ray diffraction imaging (4–6). One such approach employs iterative projection algorithms to recover the lost phase information, and thereby a real-space image, from the oversampled diffraction intensity of a compact object (7–9). However, this phase retrieval problem is only generally unique for two or three dimensions.

In one dimension, phase retrieval for a convex object is unique if all of the zeros of its Fourier modulus are real (10, 11). In fact, one-dimensional phase retrieval has been reported to reliably recover the strain profile of a thin film (12), density fluctuations near thin surfaces or interfaces (13–15), the amplitude and phase of ultrashort optical pulses (16), and the spatial distribution of the critical current in a superconducting Josephson junction (17–19). Uniqueness can be enforced if the phase of a few data points in the time domain are known (20), or if two different signals are interfered before being recorded (21). In most physical cases, the number of complex zeros is at least finite, leading to a countable number of possible solutions (10, 22, 23). It is not possible to determine if a unique solution exists by looking at the measured intensity distribution alone. Multiple trials of a phasing algorithm with different random initial conditions are necessary to test the fidelity of the recovered image (7, 8). If multiple solutions exist, the algorithm will recover each of the possible solutions; thus, the problem becomes determining which of the recovered images could be the correct representation of the object.

The present article proposes determining the correct image by attempting to splice together a movie of an object that is evolving in response to an experimental parameter. The solution set is then constrained by finding the series of images that show a logical causal progression. This approach is demonstrated by recovering the light-induced magnetic-order dynamics in a correlated electron thin film from time-resolved resonant soft X-ray diffraction measurements. In this case, it affirms the recovered solutions and resolves ambiguities in the relative object placement between frames. In some ways, the added time constraint is analogous to that imposed when recovering the wave form of ultrashort optical pulses from frequency-resolved optical gating (FROG) (24–27). However, the difference is that the FROG spectrogram represents multiple time-windowed measurements of a single light pulse, while time splicing uses similarities found in independent observations of an evolving object.

Phase transitions in materials, especially those with strong electronic correlations, often involve intertwined atomic, electronic, and spin degrees of freedom. Systematic time-resolved resonant X-ray diffraction studies have probed the evolution of the spatial average of these factors in response to optical stimuli (28–31). However, little is understood about the nonequilibrium spatial evolution of these driven transitions. One interesting example of such a spatially heterogeneous transformation is the reported demagnetization and electronic perturbative fronts launched at the interface of a LaAlO₃/NdNiO₃ (LAO/NNO) heterostructure after midinfrared excitation (32–34). The demagnetization front induced by lattice excitation of the substrate was found to travel at supersonic speed, suggesting electronic origins. However, this result came from fitting a time series of Bragg peak profiles to a model for the front propagation that could have introduced bias. To test this result, I have applied coherent diffraction imaging to recover the magnetic-order dynamics in the film without any a priori assumptions.

The noncollinear antiferromagnetic (AFM) structure of NNO in the insulating state has been determined by resonant soft X-ray diffraction (35, 36) and is shown in Fig. 1. In this structure, the magnetic moments at the Ni sites within (111) planes are aligned along either the [111] or [−1−12] directions. The alignment rotates by 90° between consecutive planes, leading to a 4× larger cubic superlattice. The quantum-mechanical mechanism that

Significance

Imaging the atomic-scale dynamics of thin films is important to develop the next generation of computer technology. Coherent diffraction imaging can provide this information for other dimensionalities, but is unreliable when applied to thin-film measurements. This paper describes an approach to solving this problem using many measurements on a system that is changing in time. As an example, a demagnetization front is imaged as it sweeps through an antiferromagnetic film at twice the speed of sound, leaving a paramagnetic state in its wake. This fast switching is initiated by a midinfrared pulse tuned to the substrate. The recovered magnetization evolution then shows the potential for control of optoelectronic switching devices by driving interface lattice dynamics.
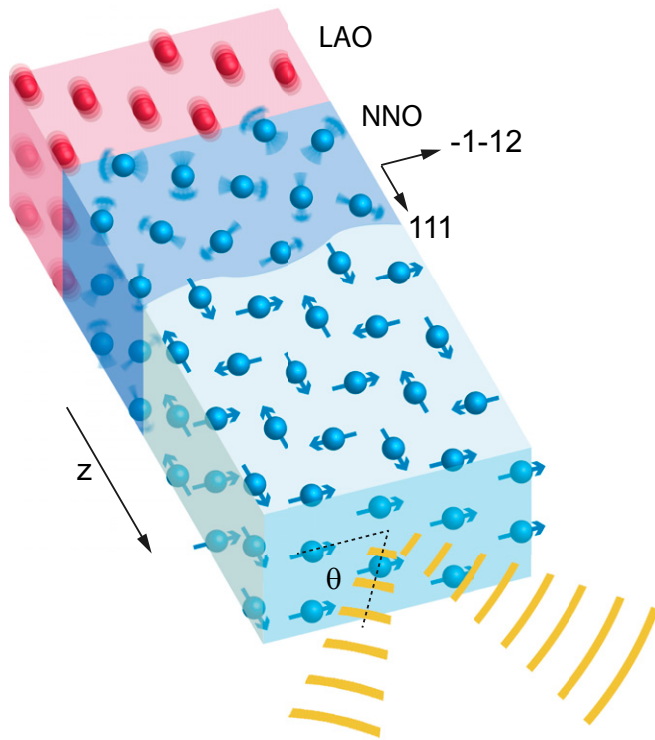
Fig. 1. Illustration of the X-ray scattering geometry and magnetization dynamics after substrate resonant mid-IR excitation. Vibrations of the LAO lattice induced by mid-IR radiation lead to a demagnetization front propagating from the interface. The noncollinear AFM structure of Ni along the [111] direction of the NNO film is shown in the top surface of the unperturbed region. The diffraction measurements were made on the front surface of the film with the incident and exiting waves illustrated as yellow stripes and the θ-scattering angle indicated. In this orientation of the NNO film, the ψ-angle is zero, as the projection of the incident X-ray beam into the surface plane is along [−1−12].

stabilizes this unusual AFM structure is currently debated, but it is believed to be related to other dynamic exchange mechanisms, where spin hopping between Ni sites is mediated by the Ni–O–Ni bonding angle (37). The resulting (1/4 1/4 1/4) diffraction peak has been shown to be solely of magnetic origin (36) without charge and orbital ordering contributions (38).

Magnetic Scattering Theory

For the experiment sketched in Fig. 1, a 30-nm-thin NNO film grown on a pseudocubic (111) LAO substrate was cooled to 40 K, well below its metal-to-insulator transition temperature of 130 K. Resonant soft X-ray diffraction θ–2θ scans of the (1/4 1/4 1/4) AFM superlattice reflection were then made at the Ni L_3 edge using p-polarized 852 eV X-rays. A polarization analyzer was not placed in the diffracted beam, so a combination of s- and p-polarized X-rays were measured. Femtosecond time-resolved measurements of the magnetic-order dynamics in the nickelate film were carried out at the SXR beamline of the Linac Coherent Light Source (32). Midinfrared and near-infrared laser excitation was used to investigate the differences between substrate lattice-driven heterogeneous magnetization dynamics and homogeneous electronically driven dynamics. The 4-mJ/cm² midinfrared (mid-IR) pump pulses were of 200-fs duration at 15-μm wavelength, which is resonant with an optical phonon of the LAO substrate, but not NNO (32). The 800-nm near-infrared pulses of equivalent fluence were 100 fs in duration. Further information about the sample and experiment has been detailed previously (32).

The measured intensity from magnetic scattering depends on the orientation of the X-ray polarization relative to the magnetic moments in the material. Starting from general equations describing the magnetic structure factor in a θ–2θ geometry (39), expressions for the measured diffraction intensities from the incident p-polarized X-rays were derived, and further details are given in *SI Appendix*. The in-plane alignment of the Ni moments allows the calculation to be reduced to the components along the scattering vector direction. The resulting structure factors for p-to-s polarization ($F_{\pi\sigma}$) and p-to-p polarization ($F_{\pi\pi}$) scattering from an ideal AFM NNO unit cell are

$$F_{\pi\sigma} = 2mf_{Ni}(\sin\theta + i\cos\theta\cos\psi), \qquad [1]$$

$$F_{\pi\pi} = 2mf_{Ni}i\sin 2\theta\sin\psi. \qquad [2]$$

Here m represents the average magnetic moment for Ni in a (111) plane, and f_{Ni} is the Ni resonant atomic scattering factor, while θ and ψ are the scattering angle and angle between the scattering plane and the [−1−12] direction, respectively. It is evident from these equations that changing the magnetic moment magnitude (m) will only influence the structure factor amplitude, while changing the orientation of the magnetic moments (θ and ψ) will influence their amplitude and phase.

If the average magnetization magnitude or orientation varies through the film, the structure factor also becomes a function of film depth, f(z). The measured intensity profile, I(q), from one of the reflected polarizations is then related to this structure factor profile by

$$I(q) = \left| \int_{-\infty}^{\infty} f(z)e^{2\pi i q z} \, dz \right|^2. \qquad [3]$$

Then, iterative phase retrieval can be used to recover the amplitude and phase of the structure factor profile from the measured intensity. The present experiment is slightly more complicated as both s- and p-polarized reflected X-rays were measured. The intensity is then given by the incoherent sum of profiles from the two polarizations. As shown in *SI Appendix*, assuming that only the average in-plane magnetization magnitude is dependent on depth, and not the magnetization orientation, a total structure factor profile can be defined that is related to the magnetization profile, m(z), by

$$f(z) = 2Nf_{Ni}\alpha(\theta,\psi)m(z)e^{i\phi(z)}, \qquad [4]$$

where

$$\alpha(\theta,\psi) = \left(\sin^2\theta + \cos^2\theta\cos^2\psi + \sin^2 2\theta\sin^2\psi\right)^{1/2}, \qquad [5]$$

and N is the number of unit cells in a scattering volume. Eq. 4 shows that the magnetization profile through the film is proportional to the amplitude of the recovered structure factor profile, as previously alluded to from inspection of the unit-cell structure factors.

In our case, the physical significance of the recovered phase profile, φ(z), is clouded by the fact that both X-ray polarizations were measured (40), and that it can have many different contributing factors. Namely, the structure factor phase is shown in the *SI Appendix* to be related to the magnetization orientation, but it can also be influenced by strain gradients in the film (12, 33, 41). As separation of these contributions to the phase requires correlating multiple measurements at different polarizations and Bragg reflections, the following analysis focuses on the magnetization profile obtained from the amplitude of the recovered structure factor profile. However, for completeness the

recovered phase profiles for all presented data are shown in *SI Appendix*, Figs. S5 and S6.

Time-Splicing Algorithm

An algorithm has been developed to obtain these depth profiles by performing iterative phase retrieval on the rocking curve measurements and checking the solution set by splicing together the results from different time delays. The general steps of the analysis are sketched in Fig. 2. First, the measured intensity was expressed in terms of the scattering vector magnitude, corrected

Fig. 2. Workflow of the magnetization depth profile reconstruction algorithm. (*Upper*) X-ray rocking curves measured with −0.5- and +1.0-ps mid-IR excitation time delays. For all time delays, 50 independent phasing trials were performed starting from diffraction peaks like those shown. (*Center*) The average raw recovered AFM order and phase, profiles, $m(z)$ and $\phi(z)$, are shown for the −0.5-ps (blue) and +1.0-ps (green) time delays. Here, discrete values of the +1.0-ps average profiles are shown, with the horizontal error bars depicting the inverse q-range spatial resolution of the profile and the shaded areas depicting the SD of the solution set. The raw set of solutions were then aligned and averaged before time splicing. (*Lower*) The final AFM order and phase profiles obtained after the average profiles were spliced together.

for background, absorption, and the Lorentz factor, and then converted to the diffraction modulus by taking its square root. The resulting modulus was used as input for a set of 50 independent phasing trials. This number was found to be a sufficient representation of the solution space as sets containing more trials were found to have the same standard deviation (SD) after alignment. A different starting point for each trial was made by combining the modulus with random initial phase values and taking its Fourier transform. The scattering factor and phase profiles were then refined using an error reduction algorithm (7, 42) that consisted of a modulus followed by a support projection operation. In all cases, 1,000 iterations of this algorithm were enough to reach convergence of the residual metric defined by

$$R = \sum \left(A_{exp}(q) - A_{rec}(q) \right)^2 \Big/ \sum A_{exp}(q)^2, \qquad [6]$$

where $A_{exp}(q)$ is the experimentally measured modulus and $A_{rec}(q)$ is the modulus of the reconstruction. Examples of the profiles obtained by averaging the converged trial results before alignment and splicing are shown in Fig. 2 (*Middle*). The 5-nm resolution of the real-space depth profile was given by the inverse of the measured range in reciprocal space and is indicted by the horizontal bars on the points shown in the figure. This is not the limit of the technique, as better resolution of the recovered profiles may be achieved by increasing the measured rocking curve angular range. A fixed support was found independently for each time delay by plotting the converged R factor from phasing trials with different support sizes between 10 and 40 nm. The accepted support size was then taken as that corresponding to the bend in the resulting L-curve (43). Further details about the support-size determination and examples of the obtained L-curves are given in *SI Appendix*.
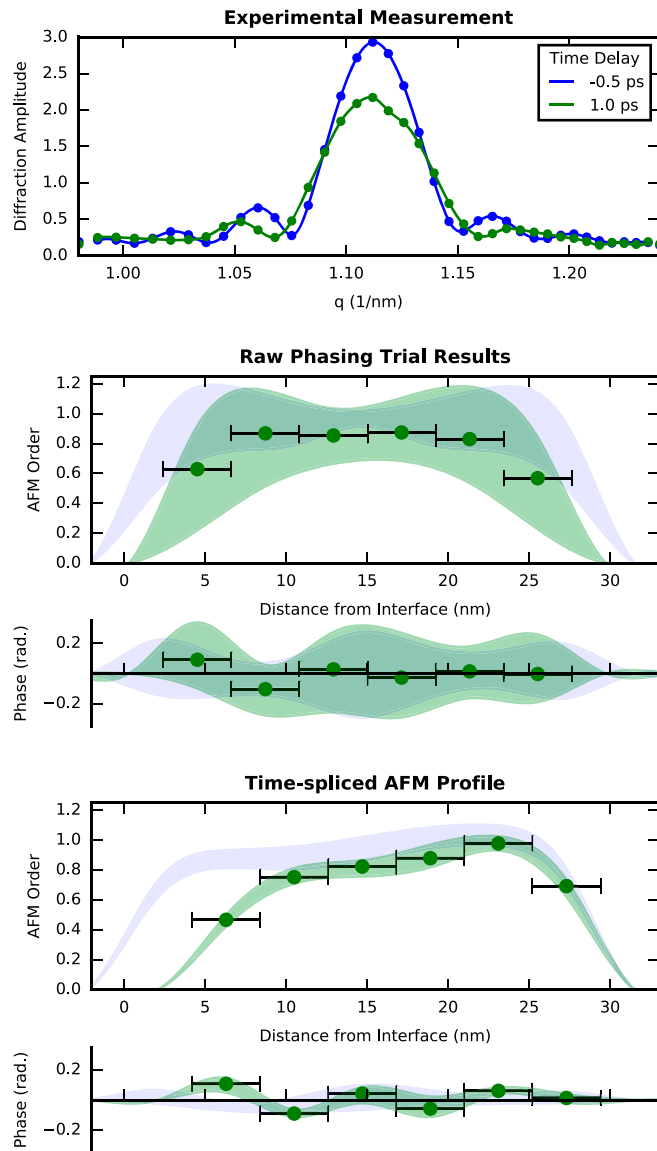
The different trial results for a given time delay were then aligned to correct for ambiguities in the solutions before averaging and assess the uniqueness of the solution set. The so-called trivial ambiguities for a complex profile, $f(z)$, are a translation and phase offset, $f(z + c)\exp(i\phi_c)$, combined with a mirror conjugation, $f^*(-z + c)\exp(i\phi_c)$ (7). The mirror-conjugation operation corresponds to an ambiguity of the orientation of the magnetization profile relative to the interface, known as the problem of determining the direction of time in short optical pulse measurements (24).

Aligning the time delays was done by first correcting for the average phase offset of the profile contained within the support. Then, a seed solution was randomly chosen from the set for translation and orientation alignment. The best translational alignment for each solution was found by minimizing the real-space correlation function
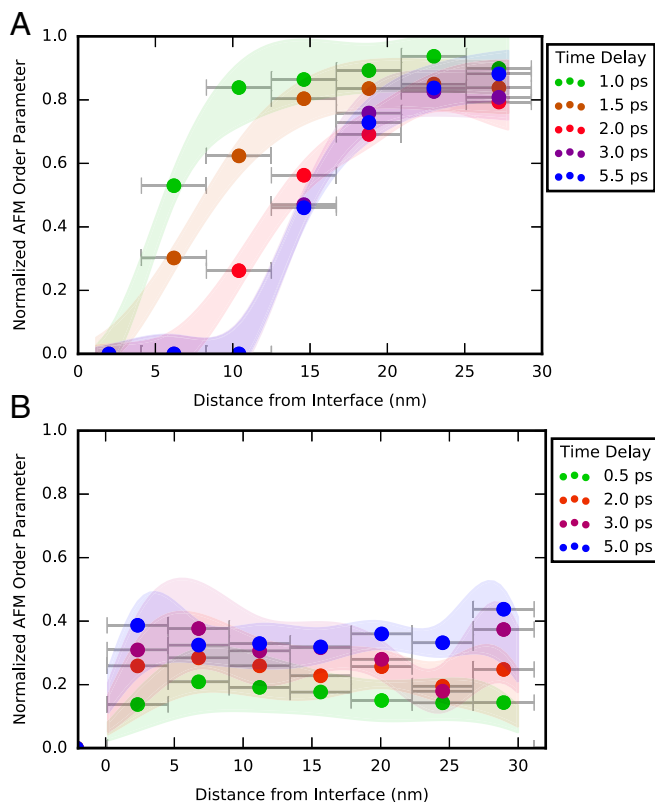
$$r_i(a) = \sum_z |f_i(z - a) - f_s(z)|^2, \qquad [7]$$

where $f_i(z)$ and $f_s(z)$ are the complex valued profiles of the ith solution and the seed solution, respectively. Then, a mirror-conjugated solution was generated, $f_i^*(-z)$, and aligned to the seed solution. This mirror solution replaced the original solution if it was found to have a lower minimum value of r_i. In this procedure, the use of the square modulus of the complex distance vector in Eq. 7 ensures that both the amplitude and phase of the recovered profiles were considered during alignment.

The uniqueness of the solution set was assessed by inspecting some of the individual trial results, as well as calculating a SD profile from the set. For each time delay, the trial solution set consisted of multiple copies of a smaller set of unique solutions. However, only slight variation was found between the unique solutions that seemed to be consistent with the noise level of the measurement. The rather uniform SD found along the depth of the aligned profiles supports this, indicating well-correlated solutions

Fig. 3. Temporal evolution of AFM ordering in the NNO film after optical excitation. (*A*) The AFM depth profiles normalized according to Eq. **8** for time delays up to 6 ps after a mid-IR pump are shown. The points represent the average and the shaded area depicts the SD from the aligned set of phasing trials. (*B*) The normalized AFM profiles of the NNO film after 800-nm excitation are also shown.

were found for all time-delay scans that were solved. Therefore, these measurements did not appear to result in multiple conflicting solutions or stagnation, which might be a consequence of using a tight fixed support (44) or related to the rather simple monotonic variation of the magnetization along the profile. The accepted set of solutions for each time delay were then averaged.

Finally, these average solutions were spliced together, allowing to check for consistencies in the recovered solutions from different time delays. The average negative time-delay solutions were taken as the initial seed profiles. Each positive time-delay average profile was then taken in series and aligned within the preceding profile. This was done again using the complex distance error metric of Eq. **7**. As shown in Figs. 2 and 3, the region of the depth profile farther than 15 nm away from the interface was found to be rather similar between time delays. This supports the claim that a reliable solution was obtained for each time step. Furthermore, the SD along the spliced profiles was reduced compared with the case of the average raw profiles because ambiguities in the position and orientation were overcome. While not needed for this case, if multiple distinct solutions had been recovered, each could be spliced into the time series, with the most likely solution being that which minimizes the real-space error metric of Eq. **7**. However, further work is needed to understand the generality of this method. Namely, before it can be applied to multilayer heterostructures, it remains to be seen if it can overcome the nonuniqueness caused by a convex support. Furthermore, the implementation of more noise-robust iterative phase-retrieval algorithms, such as the modified difference map algorithm (45), could improve its applicability to noisy data.

Results and Discussion

Fig. 3*A* shows the time evolution of the reconstructed AFM ordering in the NNO film for time delays up to 5.5 ps after mid-IR excitation. Here the AFM order parameter depth profiles, $m_t(z)$, have been normalized to that found at negative time delay, $m_{t_0}(z)$, according to

$$\hat{m}_t(z) = m_t(z)/m_{t_0}(z). \qquad [8]$$

It is seen that after only 1 ps, the AFM ordering at the interface has already disappeared. As time progresses, a front that destroys the AFM ordering propagates into the film. After 3 ps, this front stagnates at a distance of 15 nm from the interface. The AFM ordering near the film surface (25 nm from the interface) is found to decrease by only 20% within the first 1.5 ps and then stagnate. As shown in *SI Appendix*, Fig. S2, the AFM ordering begins to slowly recover after 22 ps—first growing back in the paramagnetic region near the interface before uniformly increasing in the film. *SI Appendix*, Fig. S4 shows that the magnetization recovery rate near the interface is 6× faster than near the free surface, suggesting that the excited magnetic states in these two regions of the film are fundamentally different. It is also worth noting that the transition region separating these two magnetization states, where there is a steep magnetization gradient in the film, is found to be consistently 10-nm thick during the front propagation, stagnation, and recovery dynamics.

AFM order depth profiles after near-IR excitation are shown in Fig. 3*B*. Within just 0.5 ps, the magnetic order is found to decrease uniformly over the entire film by 80%. This fast uniform reduction of the AFM ordering fits with a mechanism of uniform absorption that causes charge exchange and disruption of the electronic configuration. The recovered profiles for later time delays (*SI Appendix*, Fig. S3) recover uniformly through the film as shown in *SI Appendix*, Fig. S4. The recovery rate for the near-infrared excitation is comparable to that found near the free surface of the mid-IR excited film. Therefore, the magnetization dynamics near
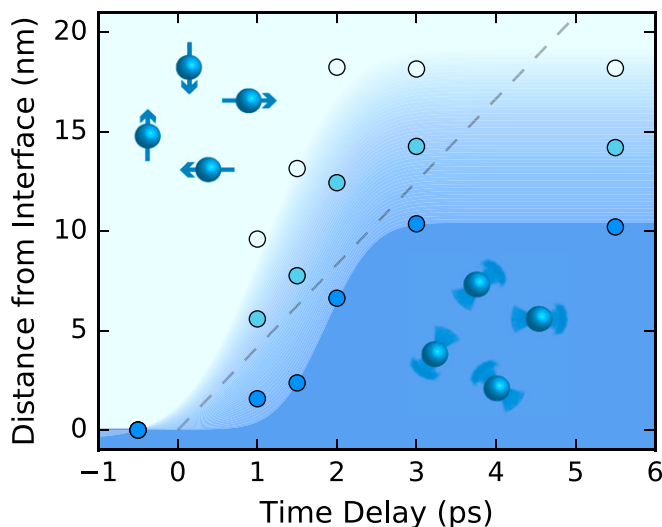
Fig. 4. Evolution of the diffuse AFM-to-PM front. The position of the initial AFM ordering disturbance, inflection point of the front, and PM front were taken from the profiles in Fig. 3*A*, and are shown as the white, light-blue, and dark-blue data points, respectively. Magnetization isolines that make up the background color gradient were then obtained by fitting error functions to such data. The color scale follows from that used for the data points. For reference, the propagation of a front traveling the speed of sound in NNO is depicted as a dashed line.

the surface of the film seem to be due to electronic excitation from absorption of the mid-IR radiation.

These dynamics are in remarkably good agreement with those obtained previously by fitting the diffraction data with an error function model of the AFM order in the film (32). However, some differences exist between the two results. For instance, in the present study, the reconstructed profiles show a decrease in the magnetization near the film surface, while this was not captured by the model chosen in the original analysis. As a result, some variation in the front position is found between the two results, but this is within the resolution of the measurements.

Fig. 4 shows magnetic-order isolines that map out the full evolution of the magnetic order after midinfrared excitation. The velocity of the propagating front can be measured using the position in the film where the AFM order drops to zero. The corresponding front velocity is a reliable measure of the transformation propagation speed, as opposed to group velocity measurements that have led to previous claims of superluminal light (46). From the slope of this line in the first 3 ps, the AFM-to-paramagnetic (PM) phase front is found to propagate at twice the speed of sound in NNO (8,200 m/s), which is in good agreement with the velocity found from the previous modeling of the data (32). Since the original study on the magnetization dynamics, other measurements on this system have found that acoustic deformation of the lattice propagates from the interface through the film slower, and an electronic disturbance sweeps through faster than the demagnetization front (33). While the mechanism driving the magnetization dynamics is still unclear, it has recently been predicted that nonlinear optical phonon coupling can modulate the exchange interaction in oxides and quickly disrupt AFM order (47). Further X-ray measurements are planned and the characteristic lengths and gradients obtained from order–disorder profiles like those shown here may be used to discern the driving mechanism.

In conclusion, time-spliced diffraction imaging has allowed for the visualization of a supersonic demagnetization front propagating in an NNO thin film. The constraints imposed by time splicing allowed for validation of the recovered profiles, and are believed to be useful to overcome cases of nonuniqueness in one-dimensional phase retrieval. I note that splicing methods are also applicable beyond time-resolved studies. As long as a transition is continuous as a function of a control parameter (e.g., magnetic field, temperature, or pressure), the recovered profiles can be spliced together to add constraints to the image recovery.

1. Qazilbash MM, et al. (2007) Mott transition in VO2 revealed by infrared spectroscopy and nano-imaging. *Science* 318:1750–1753.
2. Sherson JF, et al. (2010) Single-atom-resolved fluorescence imaging of an atomic Mott insulator. *Nature* 467:68–72.
3. Knoll A, et al. (2004) Direct imaging and mesoscale modelling of phase transitions in a nanostructured fluid. *Nat Mater* 3:886–891.
4. von Korff Schmising C, et al. (2014) Imaging ultrafast demagnetization dynamics after a spatially localized optical excitation. *Phys Rev Lett* 112:217203.
5. Clark JN, et al. (2013) Ultrafast three-dimensional imaging of lattice dynamics in individual gold nanocrystals. *Science* 341:56–59.
6. Barty A, et al. (2008) Ultrafast single-shot diffraction imaging of nanoscale dynamics. *Nat Photonics* 2:415–419.
7. Fienup JR (1978) Reconstruction of an object from the modulus of its Fourier transform. *Opt Lett* 3:27–29.
8. Miao J, Sayre D, Chapman HN (1998) Phase retrieval from the magnitude of the Fourier transforms of nonperiodic objects. *J Opt Soc Am A Opt Image Sci Vis* 15:1662–1669.
9. Marchesini S (2007) A unified evaluation of iterative projection algorithms for phase retrieval. *Rev Sci Instrum* 78:011301, and erratum (2007) 78:049901.
10. Walther A (1963) The question of phase retrieval in optics. *Opt Acta Int J Opt* 10:41–49.
11. Hofstetter E (1964) Construction of time-limited functions with specified autocorrelation functions. *IEEE Trans Inf Theory* 10:119–126.
12. Vartanyants I, Ern C, Donner W, Dosch H, Caliebe W (2000) Strain profiles in epitaxial films from x-ray Bragg diffraction phases. *Appl Phys Lett* 77:3929–3931.
13. Robinson IK, et al. (1999) Coherent x-ray diffraction imaging of silicon oxide growth. *Phys Rev B* 60:9965–9972.
14. Bengu E, Salud M, Marks LD (2001) Model-independent inversion of x-ray or neutron reflectivity data. *Phys Rev B* 63:195414.
15. Blasie JK, Zheng S, Strzalka J (2003) Solution to the phase problem for specular x-ray or neutron reflectivity from thin films on liquid surfaces. *Phys Rev B* 67:224201.
16. Naganuma K, Mogi K, Yamada H (1989) General method for ultrashort light pulse chirp measurement. *IEEE J Quantum Electron* 25:1225–1233.
17. Nesher O, Ribak EN (1997) Retrieval of critical current distribution in small Josephson junctions. *Appl Phys Lett* 71:1249–1251.
18. Carmody M, Landree E, Marks L, Merkle K (1999) Determination of the current density distribution in Josephson junctions. *Physica C Supercond* 315:145–153.
19. Carmody M, Marks LD, Merkle KL (2002) Current transport along grain boundaries in d-wave superconductors. *Physica C Supercond* 370:228–238.
20. Beinert R, Plonka G (2017) Enforcing uniqueness in one-dimensional phase retrieval by additional signal information in time domain. *Appl Comput Harmon Anal*, 10.1016/j.acha.2016.12.002.
21. Raz O, et al. (2011) Vectorial phase retrieval for linear characterization of attosecond pulses. *Phys Rev Lett* 107:133902.
22. Millane RP (1990) Phase retrieval in crystallography and optics. *J Opt Soc Am A* 7:394–411.
23. Beinert R, Plonka G (2015) Ambiguities in one-dimensional discrete phase retrieval from Fourier magnitudes. *J Fourier Anal Appl* 21:1169–1198.
24. Kane DJ, Trebino R (1993) Characterization of arbitrary femtosecond pulses using frequency-resolved optical gating. *IEEE J Quantum Electron* 29:571–579.
25. Trebino R, Kane DJ (1993) Using phase retrieval to measure the intensity and phase of ultrashort pulses: Frequency-resolved optical gating. *J Opt Soc Am A* 10:1101–1111.
26. DeLong KW, Trebino R (1994) Improved ultrashort pulse-retrieval algorithm for frequency-resolved optical gating. *J Opt Soc Am A Opt Image Sci Vis* 11:2429–2437.
27. Trebino R, et al. (1997) Measuring ultrashort laser pulses in the time-frequency domain using frequency-resolved optical gating. *Rev Sci Instrum* 68:3277–3295.
28. Chuang YD, et al. (2013) Real-time manifestation of strongly coupled spin and charge order parameters in stripe-ordered La(1.75)Sr(0.25)NiO(4) nickelate crystals using time-resolved resonant x-ray diffraction. *Phys Rev Lett* 110:127404.
29. Först M, et al. (2014) Melting of charge stripes in vibrationally driven La1.875Ba0.125CuO4: Assessing the respective roles of electronic and lattice order in frustrated superconductors. *Phys Rev Lett* 112:157002.
30. Johnson SL, et al. (2012) Femtosecond dynamics of the collinear-to-spiral antiferromagnetic phase transition in CuO. *Phys Rev Lett* 108:037203.
31. Kubacka T, et al. (2014) Large-amplitude spin dynamics driven by a THz pulse in resonance with an electromagnon. *Science* 343:1333–1336.
32. Först M, et al. (2015) Spatially resolved ultrafast magnetic dynamics initiated at a complex oxide heterointerface. *Nat Mater* 14:883–888.
33. Först M, et al. (2017) Multiple supersonic phase fronts launched at a complex-oxide heterointerface. *Phys Rev Lett* 118:027401.
34. Caviglia AD, et al. (2012) Ultrafast strain engineering in complex oxide heterostructures. *Phys Rev Lett* 108:136801.
35. Scagnoli V, et al. (2006) Role of magnetic and orbital ordering at the metal-insulator transition in NdNiO3. *Phys Rev B* 73:100409.
36. Scagnoli V, et al. (2008) Induced noncollinear magnetic order of Nd3+ in NdNiO3 observed by resonant soft x-ray diffraction. *Phys Rev B* 77:115138.
37. Middey S, et al. (2016) Physics of ultrathin films and heterostructures of rare-Earth nickelates. *Annu Rev Mater Res* 46:305–334.
38. Scagnoli V, et al. (2005) Charge disproportionation and search for orbital ordering in NdNiO3 by use of resonant x-ray diffraction. *Phys Rev B* 72:155111.
39. Hill JP, McMorrow DF (1996) X-ray resonant exchange scattering: Polarization dependence and correlation function. *Acta Crystallogr A* 52:236–244.
40. Millane RP, Arnal R, Chen J (2015) Phase retrieval for multiple objects. *Image Reconstruction from Incomplete Data VIII* (Proc. SPIE 9600, San Diego). Available at http://dx.doi.org/10.1117/12.2187631. Accessed December 18, 2017.
41. Robinson I, Harder R (2009) Coherent X-ray diffraction imaging of strain at the nanoscale. *Nat Mater* 8:291–298.
42. Gerchberg R, Saxton W (1972) A practical algorithm for the determination of the phase from image and diffraction plane pictures. *Optik (Stuttg)* 35:237–246.
43. Hansen PC (1992) Analysis of discrete ill-posed problems by means of the L-curve. *SIAM Rev* 34:561–580.
44. Fienup JR (1987) Reconstruction of a complex-valued object from the modulus of its Fourier transform using a support constraint. *J Opt Soc Am A* 4:118–123.
45. Loh N-TD, Eisebitt S, Flewett S, Elser V (2010) Recovering magnetization distributions from their noisy diffraction data. *Phys Rev E Stat Nonlin Soft Matter Phys* 82:061128.
46. Milonni P (2004) *Fast Light, Slow Light and Left-Handed Light* (Taylor & Francis London), pp 25–58.
47. Fechner M, et al. (2017) Magnetophononics: Ultrafast spin control through the lattice. Available at https://arxiv.org/abs/1707.03216. Accessed December 18, 2017.